Article

FET PET Radiomics for Differentiating Pseudoprogression from Early Tumor Progression in Glioma Patients Post-Chemoradiation

Philipp Lohmann [1,2,*], **Mai A. Elahmadawy** [1,3], **Robin Gutsche** [1,4], **Jan-Michael Werner** [5], **Elena K. Bauer** [5], **Garry Ceccon** [5], **Martin Kocher** [1,2,6], **Christoph W. Lerche** [1], **Marion Rapp** [7], **Gereon R. Fink** [1,5], **Nadim J. Shah** [1,8,9], **Karl-Josef Langen** [1,10,11] and **Norbert Galldiks** [1,5,6]

1   Institute of Neuroscience and Medicine (INM-3, -4, -11), Research Center Juelich, 52425 Juelich, Germany; mai.elahmadawy@nci.cu.edu.eg (M.A.E.); r.gutsche@fz-juelich.de (R.G.); m.kocher@fz-juelich.de (M.K.); c.lerche@fz-juelich.de (C.W.L.); g.r.fink@fz-juelich.de (G.R.F.); n.j.shah@fz-juelich.de (N.J.S.); k.j.langen@fz-juelich.de (K.-J.L.); n.galldiks@fz-juelich.de (N.G.)
2   Department of Stereotaxy and Functional Neurosurgery, Faculty of Medicine and University Hospital Cologne, University of Cologne, 50937 Cologne, Germany
3   Department of Nuclear Medicine, National Cancer Institute (NCI), Cairo University, 11796 Cairo, Egypt
4   RWTH Aachen University, 52062 Aachen, Germany
5   Department of Neurology, Faculty of Medicine and University Hospital Cologne, University of Cologne, 50937 Cologne, Germany; jan-michael.werner@uk-koeln.de (J.-M.W.); elena.bauer@uk-koeln.de (E.K.B.); garry.ceccon@uk-koeln.de (G.C.)
6   Center for Integrated Oncology (CIO), Universities Aachen, Bonn, Duesseldorf and Cologne, 50937 Cologne, Germany
7   Department of Neurosurgery, University of Duesseldorf, 40255 Duesseldorf, Germany; marion.rapp@med.uni-duesseldorf.de
8   Department of Neurology, University Hospital RWTH Aachen, 52074 Aachen, Germany
9   JARA-BRAIN-Translational Medicine, 52074 Aachen, Germany
10 Department of Nuclear Medicine, University Hospital RWTH Aachen, 52074 Aachen, Germany
11 Center for Integrated Oncology (CIO), Universities Aachen, Bonn, Duesseldorf and Cologne, 52074 Aachen, Germany
*   Correspondence: p.lohmann@fz-juelich.de

check for updates

Simple Summary: Following chemoradiation with alkylating agents in glioma patients, structural magnetic resonance imaging (MRI) may suggest tumor progression which subsequently improves during the course of the disease without any treatment change. This phenomenon has been termed pseudoprogression. Despite advances in medical imaging, a reliable diagnosis of pseudoprogression remains a challenging task. Radiomics is a subdiscipline of artificial intelligence and allows the identification and extraction of imaging features from various routine imaging modalities. These features can be used for the generation of mathematical models to improve diagnostics in patients with brain tumors. The present study highlights the potential of radiomics obtained from amino acid positron emission tomography (PET) for the diagnosis of pseudoprogression. In 34 patients with suspicious MRI early after chemoradiation completion, our radiomics model correctly identified all patients with pseudoprogression.

Abstract: Currently, a reliable diagnostic test for differentiating pseudoprogression from early tumor progression is lacking. We explored the potential of O-(2-[^{18}F]fluoroethyl)-L-tyrosine (FET) positron emission tomography (PET) radiomics for this clinically important task. Thirty-four patients (isocitrate dehydrogenase (IDH)-wildtype glioblastoma, 94%) with progressive magnetic resonance imaging (MRI) changes according to the Response Assessment in Neuro-Oncology (RANO) criteria within the first 12 weeks after completing temozolomide chemoradiation underwent a dynamic FET PET

scan. Static and dynamic FET PET parameters were calculated. For radiomics analysis, the number of datasets was increased to 102 using data augmentation. After randomly assigning patients to a training and test dataset, 944 features were calculated on unfiltered and filtered images. The number of features for model generation was limited to four to avoid data overfitting. Eighteen patients were diagnosed with early tumor progression, and 16 patients had pseudoprogression. The FET PET radiomics model correctly diagnosed pseudoprogression in all test cohort patients (sensitivity, 100%; negative predictive value, 100%). In contrast, the diagnostic performance of the best FET PET parameter (TBR_{max}) was lower (sensitivity, 81%; negative predictive value, 80%). The results suggest that FET PET radiomics helps diagnose patients with pseudoprogression with a high diagnostic performance. Given the clinical significance, further studies are warranted.

Keywords: machine learning; artificial intelligence; textural features; amino acid PET

---

1. Introduction

Pseudoprogression is a phenomenon characterized by progressive enhancing lesions on structural magnetic resonance imaging (MRI) unrelated to tumor progression. These findings either remain stable or ultimately regress on follow-up MRI without any change of treatment [1]. Pseudoprogression typically occurs within the first 12 weeks after completing radiotherapy in patients with glioblastoma [2–4]. This time-dependent definition has also been incorporated into the criteria defined by the Response Assessment in Neuro-Oncology (RANO) Working Group [2]. Importantly, overlooking pseudoprogression bears the risk of a premature termination of an effective treatment, potentially negatively impacting survival.

Pseudoprogression is caused by local tissue reactions following chemoradiation, resulting in a partial breakdown of the blood-brain barrier, thereby imitating tumor progression [4,5]. A reliable diagnosis of pseudoprogression based on contrast-enhanced MRI alone remains challenging [6,7]. To overcome this problem, several advanced imaging modalities, such as perfusion- and diffusion-weighted MR imaging (PWI, DWI), MR spectroscopy, and static and dynamic parameters derived from amino acid positron emission tomography (PET), were evaluated [6,8–10]. However, due to the long acquisition time, dynamic amino acid PET cannot be easily implemented in clinical routine [11–13]. Furthermore, the comparability of PWI, DWI, and MR spectroscopy results is hampered by the variable levels of standardization across many centers in terms of data acquisition and post-processing [8]. Therefore, a diagnostic test for reliably differentiating pseudoprogression from early tumor progression is lacking.

More recently, radiomics has gained increasing attention in medical imaging and also in the field of neurooncology [14]. As a subdiscipline of artificial intelligence and machine learning, radiomics aims at the computation, identification, and extraction of quantitative imaging features from routinely acquired imaging data and the generation of predictive or prognostic models. Predominantly, MR studies have already demonstrated the potential of radiomics for the prediction of molecular markers, such as the isocitrate dehydrogenase (IDH) genotype [15–17] or O^6-methylguanine-DNA methyltransferase (MGMT) promoter methylation [18–20], the assessment of prognosis in patients with newly diagnosed glioblastoma [21], and for the differentiation of radiation-induced changes predominantly after radiosurgery from local tumor relapse in patients with brain metastases [22–24].

Concerning the differentiation of pseudoprogression from tumor progression, initial studies suggested the potential of MRI radiomics for this challenging task [25,26]. Although its spatial resolution is inferior, and its availability is lower, the acceptance and the application of PET in patients with brain tumors have steadily increased over the past years [27,28]. In contrast to the widely used PET tracer 2-deoxy-2-[^{18}F]fluoro-D-glucose, the uptake of radiolabeled amino acids in normal brain tissue is low. The high uptake of amino acid PET tracers in both gliomas and brain metastases is

predominantly caused by an increased transport of large neutral amino acids using the L-type amino acid transporter system (LAT1 and 2) [29–33]. Hence, brain tumors can be depicted with a high tumor-to-background contrast [6]. Moreover, the uptake of amino acid tracers is independent of the blood-brain barrier [34]. In neurooncology, amino acid PET has demonstrated its additional diagnostic value in patients with glioblastoma for various indications, such as biopsy guidance and treatment planning [35–38], response assessment [39,40], and prognostication in patients with newly diagnosed glioma [41,42].

The RANO Working Group and the European Association of Neuro-Oncology (EANO) advocate the use of PET imaging in patients with brain tumors in addition to MRI at all stages of the disease [43,44]. Initial studies demonstrated that amino acid PET radiomics using the tracer O-(2-[^{18}F]fluoroethyl)-L-tyrosine (FET), either as a single modality or in combination with anatomical MRI, encodes valuable diagnostic information in patients with glioma for the prediction of the IDH genotype, the differentiation between radiation injury and recurrent brain metastases, and the assessment of prognosis in newly diagnosed glioma patients [17,24,45]. Thus, the goal of the present study was to evaluate the potential of FET PET radiomics for the diagnosis of pseudoprogression.

2. Patients and Methods

2.1. Patients

Thirty-four patients (mean age, 57 ± 12 years; age range, 24–79 years; *n* = 13 females) with newly diagnosed, histomolecularly characterized glioma according to the current WHO classification of Tumors of the Central Nervous System [46] (*n* = 32 WHO grade IV glioblastoma, IDH wildtype; *n* = 1 WHO grade IV glioblastoma, IDH mutant; *n* = 1 WHO grade III anaplastic astrocytoma, IDH wildtype) were retrospectively included in the study. Table 1 presents details of the patient cohort.

Macroscopic resections were performed in 26 patients, and eight patients received biopsies. Based on the early postoperative MRI performed within the first 48 h, 13 resections were rated as complete, and 13 were incomplete. According to the RANO criteria [2], in all patients, the first MRI within 12 weeks after completion of chemoradiation with temozolomide (according to European Organization for Research and Treatment of Cancer (EORTC) trial 22981/26981 [47]) was suspicious for tumor progression, i.e., enlargement of contrast-enhancing lesions of more than 25% or new contrast-enhancing lesions inside the radiation field. Subsequently, all patients were additionally investigated using dynamic FET PET within the following 7–10 days. Progression-free survival (PFS) was defined as the time interval from initial histomolecular diagnosis until diagnosis of the first tumor progression or recurrence. Overall survival time (OS) was defined as the time interval from initial histomolecular diagnosis to the date of death.

2.2. Ethics Statement

The study adheres to the standards established in the declaration of Helsinki. The local ethics committees approved the retrospective analysis of the data. All patients had provided written informed consent before each FET PET investigation.

2.3. Determination of the IDH Genotype and MGMT Promoter Methylation Status

The IDH mutation status was assessed by the IDH1R132H protein expression level evaluated by immunohistochemistry [48,49]. If immunostaining was negative, IDH was directly sequenced. The 1p/19q co-deletion status was analyzed by fluorescence in situ hybridization [50]. For evaluating the MGMT promoter methylation status using a methylation-specific polymerase chain reaction (PCR) [51], DNA extraction was performed from formalin-fixed and paraffin-embedded tissue samples containing tumor tissue with a histologically estimated tumor cell content of more than 80%.

Table 1. Overview of the patient cohort.

#	Gender	Age	Initial Diagnosis	IDH Genotype	MGMT Promoter Methylation	EoR	Weeks Since Last Radiation	FU Diagnosis	Confirmation of FU Diagnosis	PFS [Months]	OS [Months]	TBR_{mean}	TBR_{max}	TTP [min]	Slope [SUV/h]
1	m	58	GBM	wt	unmeth	PR	6	EP	Histomolecular	4	9	1.8	1.9	12.5	−0.4
2	m	61	GBM	wt	unmeth	CR	4	EP	Histomolecular	5	5 *	2.1	2.4	37.5	0.4
3	m	52	GBM	wt	unmeth	PR	4	EP	Histomolecular	5	15	2.2	2.8	37.5	1.1
4	m	69	GBM	wt	unmeth	PR	8	EP	Histomolecular	6	12	1.9	1.9	22.5	0.3
5	f	43	GBM	wt	unmeth	CR	8	EP	Follow-up	5	24 *	2.0	2.5	32.5	0.3
6	m	52	GBM	wt	unmeth	CR	7	EP	Follow-up	5	16	1.9	2.3	32.5	0.6
7	m	72	GBM	wt	unmeth	B	5	EP	Follow-up	4	7	2.2	3.7	18.5	−0.8
8	m	51	GBM	wt	meth	PR	6	EP	Histomolecular	5	22 *	2.5	3.9	12.5	−1.9
9	m	44	GBM	wt	unmeth	CR	3	EP	Follow-up	3	9	1.9	2.6	37.5	1.3
10	m	61	GBM	wt	unmeth	B	8	EP	Follow-up	5	6 *	2.2	2.8	27.5	−0.2
11	m	57	GBM	wt	unmeth	B	5	EP	Follow-up	2	2 *	2.1	2.8	18.5	−1.5
12	m	42	GBM	wt	meth	CR	12	EP	Follow-up	5	34	2.1	2.5	15.5	0.1
13	m	79	GBM	wt	n.a.	CR	12	EP	Histomolecular	n.a.	6 *	1.9	1.9	22.5	0.1
14	m	76	GBM	wt	meth	B	4	EP	Follow-up	4	6	2.0	2.6	18.5	−0.2
15	f	52	GBM	wt	meth	PR	8	EP	Follow-up	5	15 *	2.0	2.0	27.5	0.2
16	m	54	GBM	wt	unmeth	PR	8	EP	Follow-up	8	10	1.8	1.8	32.5	0.9
17	m	69	GBM	wt	meth	B	1	EP	Follow-up	4	4	1.9	2.1	27.5	0.9
18	f	52	GBM	wt	unmeth	PR	4	EP	Follow-up	8	11 *	2.6	3.5	37.5	1.0
19	f	71	GBM	wt	meth	PR	3	PSP	Histomolecular	12	21	1.8	1.8	37.5	0.4
20	f	76	GBM	wt	meth	CR	8	PSP	Histomolecular	20	20 *	1.9	2.2	22.5	−0.3
21	f	58	GBM	wt	unmeth	PR	8	PSP	Follow-up	24	38	2.0	2.1	22.5	−0.1
22	m	50	GBM	wt	unmeth	CR	4	PSP	Follow-up	16	23	1.9	2.0	37.5	1.0
23	m	34	GBM	wt	meth	PR	8	PSP	Follow-up	60	65 *	1.8	1.8	37.5	0.4
24	f	48	GBM	wt	n.a.	CR	8	PSP	Histomolecular	n.a.	14 *	1.9	1.9	27.5	−0.5
25	f	64	GBM	wt	meth	CR	4	PSP	Follow-up	n.a.	50	1.7	1.7	37.5	1.2
26	f	66	GBM	wt	unmeth	B	12	PSP	Follow-up	10	12	2.3	3.0	22.5	−0.7
27	m	66	GBM	wt	meth	B	12	PSP	Follow-up	16	23 *	2.2	2.5	27.5	0.4
28	f	49	GBM	wt	unmeth	PR	6	PSP	Follow-up	10	11 *	1.9	2.2	27.5	0.0
29	f	24	AA	wt	unmeth	B	11	PSP	Follow-up	8	12 *	2.1	2.4	18.5	−0.5
30	f	51	GBM	wt	unmeth	CR	8	PSP	Follow-up	8	18	1.8	1.8	27.5	0.6
31	m	44	GBM	wt	unmeth	PR	10	PSP	Follow-up	6	12	1.9	1.9	32.5	0.2
32	m	65	GBM	wt	meth	CR	6	PSP	Follow-up	11	13 *	1.8	1.8	37.5	0.9
33	f	68	GBM	wt	unmeth	PR	9	PSP	Follow-up	10	10 *	1.8	1.8	37.5	0.9
34	m	48	GBM	mut	meth	CR	6	PSP	Follow-up	24 *	24 *	1.8	1.8	37.5	0.5

AA = anaplastic astrocytoma; B = biopsy; CR = complete resection; EOR = extent of resection; EP = early tumor progression; f = female; FU = follow-up; GBM = glioblastoma; IDH = isocitrate dehydrogenase; m = male; meth = MGMT promoter methylated; MGMT = O^6-methylguanine-DNA methyltransferase; mut = mutant; n.a. = not available; OS = overall survival; PFS = progression-free survival; PR = partial resection; PSP = pseudoprogression; TBR_{max}, TBR_{mean} = maximum and mean tumor-to-brain ratio; TTP = time-to-peak; wt = wildtype; * = censored.

2.4. Diagnosis of Pseudoprogression and Early Tumor Progression

The criteria described by Young and colleagues [52] were used for the diagnosis of pseudoprogression and early tumor progression. Compared to the initial MRI, progressive enhancing or newly appearing lesions within 12 weeks after completion of chemoradiation with temozolomide were classified as either pseudoprogression or early tumor progression based on pathology after repeated tumor resection or biopsy, or, by clinicoradiological follow-up assessed every 8–12 weeks. In the cases without neuropathological confirmation, pseudoprogression was diagnosed if (i) the imaging findings regressed or remained stable during follow-up MRI, (ii) no change in treatment was required for at least six months after completion of chemoradiation with concurrent temozolomide, and (iii) the patient was clinically stable. Early tumor progression was diagnosed if MRI changes were associated with clinical deterioration and prompted a change in treatment.

2.5. FET PET Imaging

The amino acid FET was produced and applied as described previously [53,54]. All patients underwent a dynamic FET PET scan from 0 to 40 min post-injection of 3 MBq of FET per kg body weight. All patients were measured on a stand-alone PET scanner (ECAT EXACT HR+, Siemens Medical Systems, Inc., Erlangen, Germany) in 3D mode (32 rings, axial field of view, 15.5 cm; spatial resolution, 5 mm full-width at half maximum) [55]. The reconstructed dynamic dataset consisted of 14 time frames (5 × 1 min; 5 × 3 min; 4 × 5 min) with a reconstructed voxel size of $2.0 \times 2.0 \times 2.4$ mm^3. A transmission scan (duration, 10 min) using three rotating line sources (^{68}Ge/^{68}Ga) was used for attenuation correction. Before iterative ordered subset expectation maximization (OSEM) image reconstruction (16 subsets, 6 iterations), data were corrected for dead time, random and scattered coincidences.

2.6. Evaluation of Static and Dynamic FET PET Parameters

The standardized uptake value (SUV) was used to normalize the FET uptake by dividing the radioactivity in the tissue by the radioactivity injected per gram of body weight. A spherical volume-of-interest (VOI) of constant size (diameter, 30 mm; volume, 14 mL) was positioned in normal-appearing brain tissue, including grey and white matter, in the contralesional hemisphere. A three-dimensional auto-contouring process using a tumor-to-brain ratio (TBR) of 1.6 or more was used for segmenting the tumor volume in the summed PET images from 20–40 min post-injection. This threshold is based on a biopsy-controlled study in which this value separated best between vital tumor and healthy brain parenchyma in FET PET [56]. The mean TBR (TBR$_{mean}$) was calculated by dividing the mean SUV of the tumor VOI by the mean SUV of the background VOI. The maximum TBR (TBR$_{max}$) was calculated by dividing the mean SUV of a spherical VOI (diameter, 16 mm; volume, 2 mL) centered on the voxel with the maximum tumor uptake by the mean SUV of the background VOI [57].

The dynamic FET parameters TTP (time in minutes from the beginning of the dynamic acquisition up to the maximum SUV of the tumor) and slope (slope of the linear regression from 20–40 min post-injection expressed in change of SUV per hour) were extracted by the application of the 2 mL spherical VOI centered on the voxel with the maximum uptake to the entire dynamic FET PET dataset. In cases with steadily increasing FET uptake without identifiable maximum uptake, the end of the dynamic PET acquisition was defined as TTP. The background VOI described above was used to generate the time-activity curve (TAC) of the unaffected brain tissue as reference. All processing steps were performed using the software PMOD (version 4.1, PMOD Technologies Ltd., Zurich, Switzerland).

2.7. Image Pre-Processing and Radiomics Feature Extraction

Before further processing, the number of available datasets for the radiomics analysis was increased using data augmentation, i.e., three different types of tumor segmentations were used for feature extraction [58]. Besides the conventional FET PET tumor VOIs based on a TBR of 1.6 or more described

above, two other sets of tumor VOIs were created using a 10% higher TBR of 1.8 and a 10% lower TBR of 1.4, respectively. Thereby, three different segmentations for each patient were created, and the number of available datasets for feature extraction and model generation was increased from 34 to 102. Before feature extraction, patients were randomly assigned to a training dataset for model training and validation and a test dataset for final model evaluation in a ratio of 70/30, with a balanced distribution of pseudoprogression and early tumor progression diagnoses.

Feature extraction was performed with the open-source Python package pyradiomics (version, 3.0) [59]. No spatial resampling of the PET images was performed. Absolute intensity resampling was performed using a bin width of 0.15, i.e., 64 bins between 0 and 10 SUV. Absolute resampling is recommended for PET studies as it mostly removes high correlations between texture features and metabolic volume that usually occur after relative resampling [60,61]. On the original image, 107 features were calculated for each VOI, including 18 first-order statistics, 14 shape features, 24 features from the grey level co-occurrence matrix (GLCM), 16 features from the grey level run length matrix (GLRLM), 16 features from the grey level size-zone matrix (GLSZM), 5 features from the neighborhood grey level different matrix (NGLDM), and 14 from the grey level dependence matrix (GLDM). A detailed mathematical description of each feature is available in the pyradiomics documentation. Furthermore, high-pass filters using the Laplacian-of-Gaussian image filter (LoG; sigma, 0.5), as well as the discrete 3-dimensional wavelet transformation with the 'coifl' wavelet and reconstruction of the higher spatial frequency content in all directions resulting in 8 different wavelet decompositions (images) were applied, and all features (except the shape features) were also calculated on the filtered images. The LoG filter and the wavelet transformation enhance the edges of images and make the feature extraction process more sensitive to small-scale changes of tissue properties [21,62,63].

In total, 944 features were calculated for each VOI (107 features on the original image, 93 features on the LoG-filtered image, and 744 features on the wavelet-transformed images (93 features on each of the 8 different wavelet decompositions).

2.8. Feature Selection

The calculation of large numbers of features on a limited number of patients poses a specific risk of overfitting and misclassifying the data. Consequently, to reduce the number of features and identify a useful and restricted subset of features for differentiating early tumor progression and pseudoprogression, recursive feature elimination using random forest classifiers was performed. To further reduce the risk of overfitting, 5-fold cross-validation was performed during model generation, and the maximum number of features for a model generation was restricted to 4, according to published recommendations [64,65].

2.9. Model Generation and Validation

The best performing machine learning model using the selected features was identified by the Python automated machine learning Tree-based Pipeline Optimization Tool (TPOT) that uses genetic programming to optimize machine learning pipelines [66]. Several different machine learning models with different hyperparameters were applied to the training dataset, and the model with the highest accuracy for differentiating between pseudoprogression and early tumor progression after 5-fold cross-validation was considered best.

2.10. Model Testing

The best performing model in the training data was applied to the test dataset, which was not involved in model training or validation and, therefore, represents an independent dataset for the evaluation of the robustness and generalizability of the model. The radiomics workflow is presented in Figure 1.
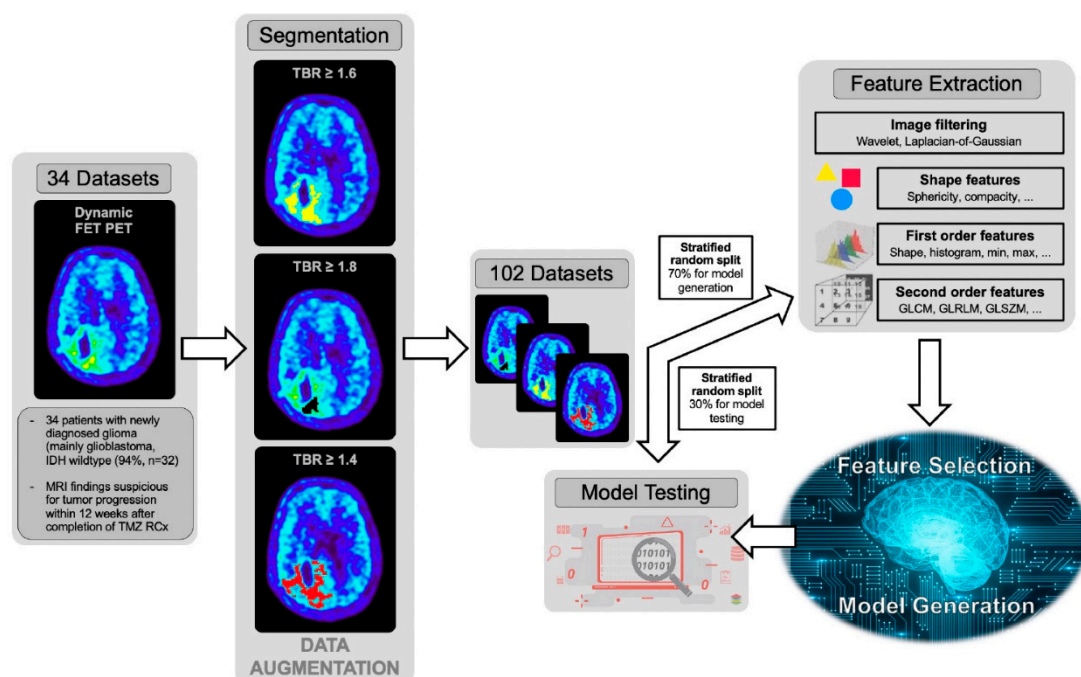
Figure 1. Radiomics workflow—Dynamic O-(2-[^{18}F]fluoroethyl)-L-tyrosine (FET) positron emission tomography (PET) measurements of 34 patients with newly diagnosed glioma (mainly glioblastoma, isocitrate dehydrogenase (IDH) wildtype (94%, *n* = 32) and magnetic resonance imaging (MRI) findings suspicious for tumor progression within 12 weeks after completion of chemoradiation with temozolomide were included in the study. Three different tumor segmentations were used to increase the number of datasets for model generation and evaluation from 34 to 102. Before feature extraction, a stratified random split of data in a ratio of 70/30 was performed. On the training datasets (*n* = 72), 107 features were calculated. Furthermore, images were filtered using the Laplacian-of-Gaussian (LoG) and the discrete 3-dimensional wavelet transformation to enhance edges in the images. In total, 944 features were calculated for each patient. Feature selection was performed by recursive feature elimination using the random forest classifiers to avoid overfitting. Furthermore, the number of features for the final model was limited to four. The best performing model on the training data was finally applied to the independent test dataset (*n* = 30).

2.11. Statistical Evaluation

Descriptive statistics are provided as mean and standard deviation or as median and range. The Mann–Whitney-U test was used for intergroup comparison. Survival analysis was performed using the log-rank test. The static and dynamic PET parameters' diagnostic performance and combinations were assessed using receiver operating characteristic (ROC) analysis. The cut-off was considered optimal when the product of specificity and sensitivity reached its maximum. The average of the hold-out predictions from the 5-fold cross-validation in each of the resampling iterations was used to evaluate the machine learning models used on the training data. The model performances in the training and the test dataset were evaluated by ROC analysis. Fisher's exact test for 2 × 2 contingency tables was applied for statistical evaluation of the parameters. *p*-values of 0.05 or less were considered statistically significant. Statistical analyses were performed using SPSS (SPSS Statistics 24, IBM, New York, USA), Microsoft Excel (Excel:Mac 2020, Version 16.35, Microsoft, Redmond, WA, USA), and SciPy [67] (version 1.4.1) for Python (version 3.7.6).

3. Results

3.1. Pseudoprogression and Early Tumor Progression

The mean time interval between completion of radiotherapy with concomitant temozolomide and the first MRI was 7 ± 3 weeks (median time, 8 weeks; range, 1–12 weeks). In all 34 patients, imaging findings on the initial MRI suggested tumor progression. Eighteen patients were diagnosed with early tumor progression, and 16 patients (47%) had pseudoprogression (Table 1). Diagnoses were based on histomolecular confirmation in 9 patients (26%) or clinicoradiological follow-up in the remaining 25 patients (74%). Patients with pseudoprogression demonstrated a significantly longer median PFS than patients with early tumor progression (11 vs. 5 months; $p < 0.001$). Additionally, pseudoprogression was associated with a significantly longer median OS (21 vs. 10 months; $p = 0.010$).

The MGMT promoter methylation status was available for 32 patients (94%). Twelve patients (35%) had tumors with a methylated MGMT promoter, and 20 patients (59%) had tumors with unmethylated MGMT promoter. There was no statistical difference between the presence of the MGMT promoter methylation in the group of patients with pseudoprogression and early tumor progression ($p = 0.411$).

3.2. Group Comparison of Static and Dynamic FET PET Parameters

The static FET PET parameters TBR_{mean} and TBR_{max} were significantly higher in the group of patients with early tumor progression compared to pseudoprogression (TBR_{mean}, 2.1 ± 0.2 vs. 1.9 ± 0.1; $p = 0.025$; TBR_{max}, 2.6 ± 0.6 vs. 2.0 ± 0.3; $p = 0.003$). The dynamic parameters TTP and slope were not significantly different between the groups.

3.3. ROC Analysis of Static and Dynamic FET PET Parameters

The static FET PET parameters TBR_{mean} and TBR_{max} yielded diagnostic accuracies of 68% (AUC, 0.73; sensitivity, 75%; specificity, 61%; cut-off, 1.95; $p = 0.045$) and 74% (AUC, 0.79; sensitivity, 81%; specificity, 67%; cut-off, 2.25; $p = 0.007$), respectively. The results from the dynamic FET PET parameters TTP and slope were not statistically significant. The highest diagnostic accuracy was achieved by combining TBR_{mean}, TBR_{max}, and the dynamic FET PET parameter TTP (accuracy, 79%; sensitivity, 69%; specificity, 89%; $p < 0.001$). Other combinations of two or more static and dynamic PET parameters did not further increase the diagnostic performance. Further details are provided in Tables 2 and 3.

Table 2. Classification results of conventional FET PET parameters for differentiating pseudoprogression from early tumor progression.

Parameter	TBR_{mean}	TBR_{max}	TTP	Slope
Sensitivity	75%	81%	75%	56%
Specificity	61%	67%	44%	61%
PPV	63%	68%	55%	56%
NPV	73%	80%	67%	61%
FNR	25%	19%	25%	44%
FPR	39%	33%	56%	39%
Accuracy	68%	74%	59%	59%
F1 Score	0.69	0.74	0.63	0.56
MCC	0.36	0.48	0.20	0.17
AUC	0.73	0.79	0.61	0.55
Cut-off	≤ 1.95	≤ 2.25	≥ 25 min	≥ 0.3 SUV/h
p-value [#]	0.045	0.007	0.297	0.492

AUC = area under the receiver operating characteristic curve; FNR = false negative rate; FPR = false positive rate; MCC = Matthews correlation coefficient; NPV = negative predictive value; PPV = positive predictive value; TBR_{max}, TBR_{mean} = maximum and mean tumor-to-brain ratio; TTP = time-to-peak; # = Fisher's exact test.

Table 3. Classification results of conventional FET PET parameter combinations for differentiating pseudoprogression from early tumor progression.

Parameter Combinations [§]	TBR$_{mean}$ + TBR$_{max}$	TBR$_{mean}$ + TTP	TBR$_{mean}$ + Slope	TBR$_{max}$ + TTP	TBR$_{max}$ + Slope	TTP + Slope	TBR$_{mean}$ + TBR$_{max}$ + TTP
Sensitivity	75%	69%	50%	69%	50%	56%	69%
Specificity	72%	78%	78%	83%	89%	61%	89%
PPV	71%	73%	67%	79%	80%	56%	85%
NPV	76%	74%	64%	75%	67%	61%	76%
FNR	25%	31%	50%	31%	50%	44%	31%
FPR	28%	22%	22%	17%	11%	39%	11%
Accuracy	74%	74%	65%	76%	71%	59%	79%
F1 Score	0.73	0.71	0.57	0.73	0.62	0.56	0.76
MCC	0.47	0.47	0.29	0.53	0.43	0.17	0.59
p-value [#]	0.015	0.014	0.151	0.005	0.023	0.492	0.001

FNR = false negative rate; FPR = false positive rate; MCC = Matthews correlation coefficient; NPV = negative predictive value; PPV = positive predictive value; TBR$_{max}$, TBR$_{mean}$ = maximum and mean tumor-to-brain ratio; TTP = time-to-peak; § = other combinations did not further increase the model performance; # = Fisher's exact test.

3.4. Performance of Machine Learning Models in the Training Dataset

According to the recursive feature elimination, the four most important parameters for differentiating early tumor progression from pseudoprogression were the shape feature *MajorAxisLength*, the two first-order features *Energy* and *Maximum*, and the second-order feature *Size-zone non-uniformity* calculated from the GLSZM. All features used in the final model were extracted from the unfiltered FET PET images.

The final model used a random forest classifier and achieved an accuracy in the training data of 86% (AUC, 0.74; sensitivity, 82%; specificity, 90%; *p* < 0.001). Further details on the performance of the machine learning model are provided in Table 4.

Table 4. Classification results of the machine learning model for differentiating pseudoprogression from early tumor progression.

	Training Data	Test Data
Number of datasets	72	30
Feature selection method	RFE (random forest)	
Number of features	4	
Classifier	Random forest	
Sensitivity	82%	100%
Specificity	90%	40%
PPV	87%	63%
NPV	85%	100%
FNR	18%	0%
FPR	10%	60%
Accuracy	86%	70%
F1 Score	0.84	0.77
MCC	0.72	0.50
AUC	0.74	0.74
p-value [#]	< 0.001	0.017

AUC = area under the receiver operating characteristic curve; FNR = false negative rate; FPR = false positive rate; MCC = Matthews correlation coefficient; NPV = negative predictive value; PPV = positive predictive value; RFE = recursive feature elimination; # = Fisher's exact test.

3.5. Performance of the Machine Learning Model in the Test Dataset

The final machine learning model showed 70% accuracy in the test dataset and correctly identified all patients with pseudoprogression (AUC, 0.74; sensitivity, 100%; specificity, 40%; *p* = 0.017). Further details on the performance of the machine learning model are provided in Table 4.

4. Discussion

The main finding of the present pilot study is that our radiomics model based on routinely acquired static FET PET scans diagnosed pseudoprogression in all patients of the test cohort correctly. Thus, the fully automated application of the proposed radiomics model based on amino acid PET has the potential to serve as a diagnostic tool for pseudoprogression in patients with equivocal MRI findings after completion of temozolomide chemoradiation. Although our model showed a lower overall diagnostic performance in the test dataset with an AUC of 0.74, the sensitivity and negative predictive value were 100%.

Several studies in glioma patients have evaluated the value of amino acid PET for differentiating early tumor progression from pseudoprogression and reported high diagnostic accuracies in the range of 79–94% [11–13,68]. Importantly, these studies combined static and dynamic FET PET parameters, which requires a costly and time-consuming dynamic PET acquisition of at least 40 min, hampering clinical implementation. In contrast, the radiomics analysis in our study uses only imaging features extracted from a 20 min static PET acquisition, which is less laborious, more economical, and already part of clinical routine in many neurooncological centers in Europe. Furthermore, the application of the developed radiomics model does not require specialized hardware and can be performed entirely automatically on a conventional computer in a few seconds. Of note, amino acid PET radiomics should not be considered a stand-alone method, but rather as an additional diagnostic information source based on routinely acquired imaging data.

Up to now, studies evaluating the potential of radiomics for differentiating early tumor progression and pseudoprogression were predominantly based on advanced MRI. For example, Kim and colleagues [25] combined structural MRI with DWI and PWI and generated a radiomics model using 12 features that could diagnose pseudoprogression in a test cohort with an AUC of 0.85. Elshafeey and co-workers [26] built a classifier using 60 radiomic features from multicentric PWI data that could diagnose pseudoprogression in a test dataset with a high diagnostic accuracy (AUC, 0.89). However, due to the large number of parameters used in these models, the interpretation is challenging, limiting its clinical acceptance.

In contrast, our radiomics model based on FET PET utilizes only four parameters, which may ameliorate its interpretation and clinical acceptance. The clinical acceptance of radiomics and its subsequent clinical translation depends mainly on the diagnostic benefit. In our opinion, easy implementation into clinical routine and improved model interpretability, which often appears complex at first glance, may contribute significantly to the clinical translation. Therefore, we concentrated on models with a small number of parameters, which makes an interpretation more straightforward and lowers the risk of overfitting considerably.

The features used in the final model of our study were (i) the shape feature *MajorAxisLength*, which yields the most extensive axis length of the VOI-enclosing ellipsoid; (ii) the histogram-derived feature *Energy,* which is a measure of the magnitude of voxel values; (iii) the histogram-derived feature *Maximum*, which represents the maximum value in the VOI; (iv) and the second-order feature *Size-zone non-uniformity* from the GLSZM, which measures the variability of size-zone volumes in the image with a lower value indicating more homogeneity. All features in the final model were extracted from the unfiltered images, and, interestingly, patients with early tumor progression showed a more heterogeneous FET uptake than patients with pseudoprogression (Figure 2). Similarly, a previous study reported that patients with recurrent brain metastases following stereotactic radiosurgery also exhibit a more heterogenous FET uptake compared to patients with radiation-induced changes [24]. To further elucidate this unclear observation, a direct comparison of radiomics features with histomolecular parameters is warranted.
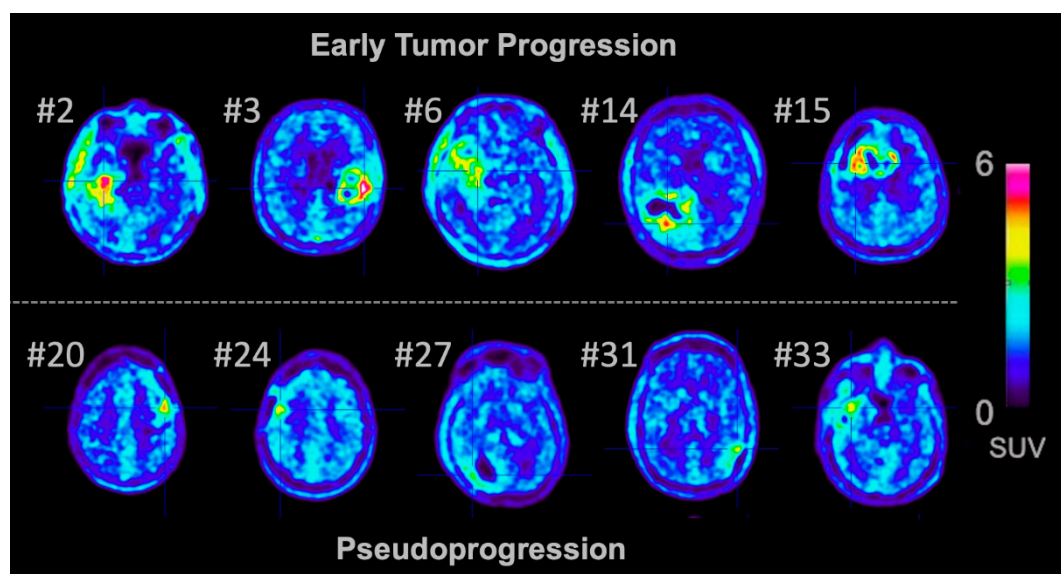
Figure 2. Representative O-(2-[^{18}F]fluoroethyl)-L-tyrosine (FET) positron emission tomography (PET) images of glioblastoma patients with early tumor progression (top row) and pseudoprogression (bottom row). Patients with pseudoprogression showed a slightly lower and more homogenous FET uptake, whereas patients with early tumor progression showed a more heterogenous FET uptake. This visual impression was also reflected by the identified radiomics parameters.

Several limitations of the study need to be discussed. The presented cohort is small, but, as we strictly adhere to the time-dependent definition of pseudoprogression, the risk of misclassification was considerably reduced and contributed to a reasonably homogenous patient collective. Additionally, using slightly different tumor segmentations, the number of datasets for the radiomics analysis, model generation, and evaluation could be increased and allowed a meaningful machine learning workflow. Furthermore, multiple segmentations limit the extent of bias introduced by the segmentation variability, thus enabling robust features to be identified [69–71].

Model robustness and generalizability were demonstrated in an independent test dataset, and the risk of overfitting was minimized by reducing the number of features to four and performing cross-validation during model training. Nevertheless, a multicenter dataset is desirable for model evaluation.

5. Conclusions

In summary, the presented FET PET radiomics model correctly diagnosed all patients with pseudoprogression in an independent test dataset without the need for costly and time-consuming dynamic FET PET scans. Thereby, this approach justifies routine clinical application. Despite the promising performance of the developed radiomics model in the test dataset, further validation of the developed model in a large multicentric dataset is necessary. Since some studies have shown a synergistic effect by combining PET and MRI radiomics [24,72], the combination of FET PET radiomics with structural, as well as advanced, MRI radiomics should also be further investigated, especially in the light of the growing number of hybrid PET/MR scanners. This pilot study results are promising and suggest an important role for FET PET radiomics in neurooncology.

Author Contributions: Conceptualization, P.L. and N.G.; data acquisition: E.K.B., M.K., J.-M.W., M.R., G.C., C.W.L., G.R.F., N.J.S., K.-J.L.; methodology, P.L., M.A.E., R.G. and N.G.; software, P.L. and R.G.; validation, P.L., R.G. and N.G.; formal analysis, P.L., M.A.E., R.G. and N.G.; writing—original draft preparation P.L. and N.G.; writing—review and editing, All; funding acquisition, P.L., K.-J.L. and N.G. All authors have read and agreed to the published version of the manuscript.

References

1. Taal, W.; Brandsma, D.; de Bruin, H.G.; Bromberg, J.E.; Swaak-Kragten, A.T.; Smitt, P.A.; van Es, C.A.; van den Bent, M.J. Incidence of early pseudo-progression in a cohort of malignant glioma patients treated with chemoirradiation with temozolomide. *Cancer* **2008**, *113*, 405–410. [CrossRef] [PubMed]

2. Wen, P.Y.; Macdonald, D.R.; Reardon, D.A.; Cloughesy, T.F.; Sorensen, A.G.; Galanis, E.; Degroot, J.; Wick, W.; Gilbert, M.R.; Lassman, A.B.; et al. Updated response assessment criteria for high-grade gliomas: Response assessment in neuro-oncology working group. *J. Clin. Oncol.* **2010**, *28*, 1963–1972. [CrossRef] [PubMed]

3. Brandsma, D.; Stalpers, L.; Taal, W.; Sminia, P.; van den Bent, M.J. Clinical features, mechanisms, and management of pseudoprogression in malignant gliomas. *Lancet Oncol.* **2008**, *9*, 453–461. [CrossRef]

4. Brandsma, D.; van den Bent, M.J. Pseudoprogression and pseudoresponse in the treatment of gliomas. *Curr. Opin. Neurol.* **2009**, *22*, 633–638. [CrossRef]

5. Galldiks, N.; Kocher, M.; Langen, K.J. Pseudoprogression after glioma therapy: An update. *Expert Rev. Neurother.* **2017**, *17*, 1109–1115. [CrossRef] [PubMed]

6. Langen, K.J.; Galldiks, N.; Hattingen, E.; Shah, N.J. Advances in neuro-oncology imaging. *Nat. Rev. Neurol.* **2017**, *13*, 279–289. [CrossRef] [PubMed]

7. Kumar, A.J.; Leeds, N.E.; Fuller, G.N.; Van Tassel, P.; Maor, M.H.; Sawaya, R.E.; Levin, V.A. Malignant gliomas: MR imaging spectrum of radiation therapy- and chemotherapy-induced necrosis of the brain after treatment. *Radiology* **2000**, *217*, 377–384. [CrossRef] [PubMed]

8. Thust, S.C.; van den Bent, M.J.; Smits, M. Pseudoprogression of brain tumors. *J. Magn. Reson. Imaging* **2018**, *48*, 571–589. [CrossRef]

9. van Dijken, B.R.J.; van Laar, P.J.; Holtman, G.A.; van der Hoorn, A. Diagnostic accuracy of magnetic resonance imaging techniques for treatment response evaluation in patients with high-grade glioma, a systematic review and meta-analysis. *Eur. Radiol.* **2017**, *27*, 4129–4144. [CrossRef]

10. Lerche, C.; Radomski, T.; Lohmann, P.; Regio-Brambilla, C.; Tellmann, L.; Scheins, J.; Rota Kops, E.; Herzog, H.; Langen, K.-J.; Shah, N.J. Clinical applicability of a mathematical model for FET PET uptake kinetics in brain tumor patients. *Eur. J. Nucl. Med. Mol. Imaging* **2019**, *46*, S231–S232.

11. Werner, J.M.; Stoffels, G.; Lichtenstein, T.; Borggrefe, J.; Lohmann, P.; Ceccon, G.; Shah, N.J.; Fink, G.R.; Langen, K.J.; Kabbasch, C.; et al. Differentiation of treatment-related changes from tumour progression: A direct comparison between dynamic FET PET and ADC values obtained from DWI MRI. *Eur. J. Nucl. Med. Mol. Imaging* **2019**, *46*, 1889–1901. [CrossRef] [PubMed]

12. Galldiks, N.; Dunkl, V.; Stoffels, G.; Hutterer, M.; Rapp, M.; Sabel, M.; Reifenberger, G.; Kebir, S.; Dorn, F.; Blau, T.; et al. Diagnosis of pseudoprogression in patients with glioblastoma using O-(2-[18F]fluoroethyl)-L-tyrosine PET. *Eur. J. Nucl. Med. Mol. Imaging* **2015**, *42*, 685–695. [CrossRef] [PubMed]

13. Kebir, S.; Fimmers, R.; Galldiks, N.; Schafer, N.; Mack, F.; Schaub, C.; Stuplich, M.; Niessen, M.; Tzaridis, T.; Simon, M.; et al. Late Pseudoprogression in Glioblastoma: Diagnostic Value of Dynamic O-(2-[18F]fluoroethyl)-L-Tyrosine PET. *Clin. Cancer Res.* **2016**, *22*, 2190–2196. [CrossRef] [PubMed]

14. Gillies, R.J.; Kinahan, P.E.; Hricak, H. Radiomics: Images Are More than Pictures, They Are Data. *Radiology* **2016**, *278*, 563–577. [CrossRef] [PubMed]

15. Shofty, B.; Artzi, M.; Ben Bashat, D.; Liberman, G.; Haim, O.; Kashanian, A.; Bokstein, F.; Blumenthal, D.T.; Ram, Z.; Shahar, T. MRI radiomics analysis of molecular alterations in low-grade gliomas. *Int J. Comput Assist. Radiol Surg.* **2018**, *13*, 563–571. [CrossRef] [PubMed]

16. Zhou, H.; Chang, K.; Bai, H.X.; Xiao, B.; Su, C.; Bi, W.L.; Zhang, P.J.; Senders, J.T.; Vallieres, M.; Kavouridis, V.K.; et al. Machine learning reveals multimodal MRI patterns predictive of isocitrate dehydrogenase and 1p/19q status in diffuse low- and high-grade gliomas. *J. Neurooncol.* **2019**, *142*, 299–307. [CrossRef]

17. Lohmann, P.; Lerche, C.; Bauer, E.K.; Steger, J.; Stoffels, G.; Blau, T.; Dunkl, V.; Kocher, M.; Viswanathan, S.; Filss, C.P.; et al. Predicting IDH genotype in gliomas using FET PET radiomics. *Sci. Rep.* **2018**, *8*, 13328. [CrossRef]

18. Li, Z.C.; Bai, H.; Sun, Q.; Li, Q.; Liu, L.; Zou, Y.; Chen, Y.; Liang, C.; Zheng, H. Multiregional radiomics features from multiparametric MRI for prediction of MGMT methylation status in glioblastoma multiforme: A multicentre study. *Eur. Radiol.* **2018**, *28*, 3640–3650. [CrossRef]

19. Xi, Y.B.; Guo, F.; Xu, Z.L.; Li, C.; Wei, W.; Tian, P.; Liu, T.T.; Liu, L.; Chen, G.; Ye, J.; et al. Radiomics signature: A potential biomarker for the prediction of MGMT promoter methylation in glioblastoma. *J. Magn. Reson. Imaging* **2018**, *47*, 1380–1387. [CrossRef]

20. Kong, Z.; Lin, Y.; Jiang, C.; Li, L.; Liu, Z.; Wang, Y.; Dai, C.; Liu, D.; Qin, X.; Wang, Y.; et al. (18)F-FDG-PET-based Radiomics signature predicts MGMT promoter methylation status in primary diffuse glioma. *Cancer Imaging* **2019**, *19*, 58. [CrossRef]

21. Kickingereder, P.; Burth, S.; Wick, A.; Gotz, M.; Eidel, O.; Schlemmer, H.P.; Maier-Hein, K.H.; Wick, W.; Bendszus, M.; Radbruch, A.; et al. Radiomic Profiling of Glioblastoma: Identifying an Imaging Predictor of Patient Survival with Improved Performance over Established Clinical and Radiologic Risk Models. *Radiology* **2016**, *280*, 880–889. [CrossRef] [PubMed]

22. Zhang, Z.; Yang, J.; Ho, A.; Jiang, W.; Logan, J.; Wang, X.; Brown, P.D.; McGovern, S.L.; Guha-Thakurta, N.; Ferguson, S.D.; et al. A predictive model for distinguishing radiation necrosis from tumour progression after gamma knife radiosurgery based on radiomic features from MR images. *Eur. Radiol.* **2018**, *28*, 2255–2263. [CrossRef] [PubMed]

23. Peng, L.; Parekh, V.; Huang, P.; Lin, D.D.; Sheikh, K.; Baker, B.; Kirschbaum, T.; Silvestri, F.; Son, J.; Robinson, A.; et al. Distinguishing True Progression From Radionecrosis After Stereotactic Radiation Therapy for Brain Metastases With Machine Learning and Radiomics. *Int. J. Radiat. Oncol. Biol. Phys.* **2018**, *102*, 1236–1243. [CrossRef] [PubMed]

24. Lohmann, P.; Kocher, M.; Ceccon, G.; Bauer, E.K.; Stoffels, G.; Viswanathan, S.; Ruge, M.I.; Neumaier, B.; Shah, N.J.; Fink, G.R.; et al. Combined FET PET/MRI radiomics differentiates radiation injury from recurrent brain metastasis. *Neuroimage Clin.* **2018**, *20*, 537–542. [CrossRef]

25. Kim, J.Y.; Park, J.E.; Jo, Y.; Shim, W.H.; Nam, S.J.; Kim, J.H.; Yoo, R.E.; Choi, S.H.; Kim, H.S. Incorporating diffusion- and perfusion-weighted MRI into a radiomics model improves diagnostic performance for pseudoprogression in glioblastoma patients. *Neuro Oncol.* **2019**, *21*, 404–414. [CrossRef]

26. Elshafeey, N.; Kotrotsou, A.; Hassan, A.; Elshafei, N.; Hassan, I.; Ahmed, S.; Abrol, S.; Agarwal, A.; El Salek, K.; Bergamaschi, S.; et al. Multicenter study demonstrates radiomic features derived from magnetic resonance perfusion images identify pseudoprogression in glioblastoma. *Nat. Commun.* **2019**, *10*, 3170. [CrossRef]

27. Najjar, A.M.; Johnson, J.M.; Schellingerhout, D. The Emerging Role of Amino Acid PET in Neuro-Oncology. *Bioengineering (Basel)* **2018**, *5*, 104. [CrossRef] [PubMed]

28. Galldiks, N.; Lohmann, P.; Albert, N.L.; Tonn, J.C.; Langen, K.J. Current status of PET imaging in neuro-oncology. *Neurooncol. Adv.* **2019**, *1*, vdz010. [CrossRef]

29. Youland, R.S.; Kitange, G.J.; Peterson, T.E.; Pafundi, D.H.; Ramiscal, J.A.; Pokorny, J.L.; Giannini, C.; Laack, N.N.; Parney, I.F.; Lowe, V.J.; et al. The role of LAT1 in (18)F-DOPA uptake in malignant gliomas. *J. Neurooncol.* **2013**, *111*, 11–18. [CrossRef]

30. Habermeier, A.; Graf, J.; Sandhofer, B.F.; Boissel, J.P.; Roesch, F.; Closs, E.I. System L amino acid transporter LAT1 accumulates O-(2-fluoroethyl)-L-tyrosine (FET). *Amino Acids* **2015**, *47*, 335–344. [CrossRef]

31. Langen, K.J.; Hamacher, K.; Weckesser, M.; Floeth, F.; Stoffels, G.; Bauer, D.; Coenen, H.H.; Pauleit, D. O-(2-[18F]fluoroethyl)-L-tyrosine: Uptake mechanisms and clinical applications. *Nucl. Med. Biol.* **2006**, *33*, 287–294. [CrossRef] [PubMed]

32. Okubo, S.; Zhen, H.N.; Kawai, N.; Nishiyama, Y.; Haba, R.; Tamiya, T. Correlation of L-methyl-11C-methionine (MET) uptake with L-type amino acid transporter 1 in human gliomas. *J. Neurooncol.* **2010**, *99*, 217–225. [CrossRef] [PubMed]

33. Papin-Michault, C.; Bonnetaud, C.; Dufour, M.; Almairac, F.; Coutts, M.; Patouraux, S.; Virolle, T.; Darcourt, J.; Burel-Vandenbos, F. Study of LAT1 Expression in Brain Metastases: Towards a Better Understanding of the Results of Positron Emission Tomography Using Amino Acid Tracers. *PLoS ONE* **2016**, *11*, e0157139. [CrossRef]

34. Galldiks, N.; Unterrainer, M.; Judov, N.; Stoffels, G.; Rapp, M.; Lohmann, P.; Vettermann, F.; Dunkl, V.; Suchorska, B.; Tonn, J.C.; et al. Photopenic defects on O-(2-[18F]-fluoroethyl)-L-tyrosine PET: Clinical relevance in glioma patients. *Neuro Oncol.* **2019**, *21*, 1331–1338. [CrossRef] [PubMed]

35. Pirotte, B.; Goldman, S.; Massager, N.; David, P.; Wikler, D.; Vandesteene, A.; Salmon, I.; Brotchi, J.; Levivier, M. Comparison of 18F-FDG and 11C-methionine for PET-guided stereotactic brain biopsy of gliomas. *J. Nucl. Med.* **2004**, *45*, 1293–1298.

36. Lohmann, P.; Stavrinou, P.; Lipke, K.; Bauer, E.K.; Ceccon, G.; Werner, J.M.; Neumaier, B.; Fink, G.R.; Shah, N.J.; Langen, K.J.; et al. FET PET reveals considerable spatial differences in tumour burden compared to conventional MRI in newly diagnosed glioblastoma. *Eur. J. Nucl. Med. Mol. Imaging* **2019**, *46*, 591–602. [CrossRef]

37. Navarria, P.; Reggiori, G.; Pessina, F.; Ascolese, A.M.; Tomatis, S.; Mancosu, P.; Lobefalo, F.; Clerici, E.; Lopci, E.; Bizzi, A.; et al. Investigation on the role of integrated PET/MRI for target volume definition and radiotherapy planning in patients with high grade glioma. *Radiother. Oncol.* **2014**, *112*, 425–429. [CrossRef]

38. Weber, D.C.; Zilli, T.; Buchegger, F.; Casanova, N.; Haller, G.; Rouzaud, M.; Nouet, P.; Dipasquale, G.; Ratib, O.; Zaidi, H.; et al. [(18)F]Fluoroethyltyrosine- positron emission tomography-guided radiotherapy for high-grade glioma. *Radiat. Oncol.* **2008**, *3*, 44. [CrossRef]

39. Ceccon, G.; Lohmann, P.; Werner, J.M.; Tscherpel, C.; Dunkl, V.; Stoffels, G.; Rosen, J.; Rapp, M.; Sabel, M.; Herrlinger, U.; et al. Early treatment response assessment using (18)F-FET PET compared to contrast-enhanced MRI in glioma patients following adjuvant temozolomide chemotherapy. *J. Nucl. Med.* **2020**. [CrossRef]

40. Galldiks, N.; Dunkl, V.; Ceccon, G.; Tscherpel, C.; Stoffels, G.; Law, I.; Henriksen, O.M.; Muhic, A.; Poulsen, H.S.; Steger, J.; et al. Early treatment response evaluation using FET PET compared to MRI in glioblastoma patients at first progression treated with bevacizumab plus lomustine. *Eur J. Nucl. Med. Mol. Imaging* **2018**, *45*, 2377–2386. [CrossRef]

41. Suchorska, B.; Jansen, N.L.; Linn, J.; Kretzschmar, H.; Janssen, H.; Eigenbrod, S.; Simon, M.; Popperl, G.; Kreth, F.W.; la Fougere, C.; et al. Biological tumor volume in 18FET-PET before radiochemotherapy correlates with survival in GBM. *Neurology* **2015**, *84*, 710–719. [CrossRef]

42. Galldiks, N.; Ullrich, R.; Schroeter, M.; Fink, G.R.; Jacobs, A.H.; Kracht, L.W. Volumetry of [(11)C]-methionine PET uptake and MRI contrast enhancement in patients with recurrent glioblastoma multiforme. *Eur J. Nucl. Med. Mol. Imaging* **2010**, *37*, 84–92. [CrossRef]

43. Albert, N.L.; Weller, M.; Suchorska, B.; Galldiks, N.; Soffietti, R.; Kim, M.M.; la Fougere, C.; Pope, W.; Law, I.; Arbizu, J.; et al. Response Assessment in Neuro-Oncology working group and European Association for Neuro-Oncology recommendations for the clinical use of PET imaging in gliomas. *Neuro Oncol.* **2016**, *18*, 1199–1208. [CrossRef] [PubMed]

44. Galldiks, N.; Langen, K.J.; Albert, N.L.; Chamberlain, M.; Soffietti, R.; Kim, M.M.; Law, I.; Le Rhun, E.; Chang, S.; Schwarting, J.; et al. PET imaging in patients with brain metastasis-report of the RANO/PET group. *Neuro Oncol.* **2019**, *21*, 585–595. [CrossRef] [PubMed]

45. Pyka, T.; Gempt, J.; Hiob, D.; Ringel, F.; Schlegel, J.; Bette, S.; Wester, H.J.; Meyer, B.; Forster, S. Textural analysis of pre-therapeutic [18F]-FET-PET and its correlation with tumor grade and patient survival in high-grade gliomas. *Eur. J. Nucl. Med. Mol. Imaging* **2016**, *43*, 133–141. [CrossRef] [PubMed]

46. Louis, D.N.; Perry, A.; Reifenberger, G.; von Deimling, A.; Figarella-Branger, D.; Cavenee, W.K.; Ohgaki, H.; Wiestler, O.D.; Kleihues, P.; Ellison, D.W. The 2016 World Health Organization Classification of Tumors of the Central Nervous System: A summary. *Acta Neuropathol.* **2016**, *131*, 803–820. [CrossRef] [PubMed]

47. Stupp, R.; Mason, W.P.; van den Bent, M.J.; Weller, M.; Fisher, B.; Taphoorn, M.J.; Belanger, K.; Brandes, A.A.; Marosi, C.; Bogdahn, U.; et al. Radiotherapy plus concomitant and adjuvant temozolomide for glioblastoma. *N. Engl. J. Med.* **2005**, *352*, 987–996. [CrossRef]

48. Capper, D.; Zentgraf, H.; Balss, J.; Hartmann, C.; von Deimling, A. Monoclonal antibody specific for IDH1 R132H mutation. *Acta Neuropathol.* **2009**, *118*, 599–601. [CrossRef]

49. Capper, D.; Weissert, S.; Balss, J.; Habel, A.; Meyer, J.; Jager, D.; Ackermann, U.; Tessmer, C.; Korshunov, A.; Zentgraf, H.; et al. Characterization of R132H mutation-specific IDH1 antibody binding in brain tumors. *Brain Pathol.* **2010**, *20*, 245–254. [CrossRef]

50. Woehrer, A.; Sander, P.; Haberler, C.; Kern, S.; Maier, H.; Preusser, M.; Hartmann, C.; Kros, J.M.; Hainfellner, J.A.; Research Committee of the European Confederation of Neuropathological Societies. FISH-based detection of 1p 19q codeletion in oligodendroglial tumors: Procedures and protocols for neuropathological practice - a publication under the auspices of the Research Committee of the European Confederation of Neuropathological Societies (Euro-CNS). *Clin. Neuropathol.* **2011**, *30*, 47–55.

51. Felsberg, J.; Rapp, M.; Loeser, S.; Fimmers, R.; Stummer, W.; Goeppert, M.; Steiger, H.J.; Friedensdorf, B.; Reifenberger, G.; Sabel, M.C. Prognostic significance of molecular markers and extent of resection in primary glioblastoma patients. *Clin. Cancer Res.* **2009**, *15*, 6683–6693. [CrossRef] [PubMed]

52. Young, R.J.; Gupta, A.; Shah, A.D.; Graber, J.J.; Zhang, Z.; Shi, W.; Holodny, A.I.; Omuro, A.M. Potential utility of conventional MRI signs in diagnosing pseudoprogression in glioblastoma. *Neurology* **2011**, *76*, 1918–1924. [CrossRef] [PubMed]

53. Hamacher, K.; Coenen, H.H. Efficient routine production of the 18F-labelled amino acid O-2-18F fluoroethyl-L-tyrosine. *Appl. Radiat. Isot.* **2002**, *57*, 853–856. [CrossRef]

54. Langen, K.J.; Bartenstein, P.; Boecker, H.; Brust, P.; Coenen, H.H.; Drzezga, A.; Grunwald, F.; Krause, B.J.; Kuwert, T.; Sabri, O.; et al. [German guidelines for brain tumour imaging by PET and SPECT using labelled amino acids]. *Nuklearmedizin* **2011**, *50*, 167–173.

55. Caldeira, L.; Kops, E.R.; Yun, S.D.; Da Silva, N.; Mauler, J.; Weirich, C.; Scheins, J.; Herzog, H.; Tellmann, L.; Lohmann, P.; et al. The Julich Experience With Simultaneous 3T MR-BrainPET: Methods and Technology. *IEEE Trans. Radiat. Plasma Med. Sci.* **2019**, *3*, 352–362. [CrossRef]

56. Pauleit, D.; Floeth, F.; Hamacher, K.; Riemenschneider, M.J.; Reifenberger, G.; Muller, H.W.; Zilles, K.; Coenen, H.H.; Langen, K.J. O-(2-[18F]fluoroethyl)-L-tyrosine PET combined with MRI improves the diagnostic assessment of cerebral gliomas. *Brain* **2005**, *128*, 678–687. [CrossRef]

57. Galldiks, N.; Stoffels, G.; Filss, C.; Rapp, M.; Blau, T.; Tscherpel, C.; Ceccon, G.; Dunkl, V.; Weinzierl, M.; Stoffel, M.; et al. The use of dynamic O-(2-18F-fluoroethyl)-l-tyrosine PET in the diagnosis of patients with progressive and recurrent glioma. *Neuro Oncol.* **2015**, *17*, 1293–1300. [CrossRef] [PubMed]

58. Lambin, P.; Leijenaar, R.T.H.; Deist, T.M.; Peerlings, J.; de Jong, E.E.C.; van Timmeren, J.; Sanduleanu, S.; Larue, R.; Even, A.J.G.; Jochems, A.; et al. Radiomics: The bridge between medical imaging and personalized medicine. *Nat. Rev. Clin. Oncol.* **2017**, *14*, 749–762. [CrossRef]

59. van Griethuysen, J.J.M.; Fedorov, A.; Parmar, C.; Hosny, A.; Aucoin, N.; Narayan, V.; Beets-Tan, R.G.H.; Fillion-Robin, J.C.; Pieper, S.; Aerts, H. Computational Radiomics System to Decode the Radiographic Phenotype. *Cancer Res.* **2017**, *77*, e104–e107. [CrossRef] [PubMed]

60. Orlhac, F.; Nioche, C.; Soussan, M.; Buvat, I. Understanding Changes in Tumor Texture Indices in PET: A Comparison Between Visual Assessment and Index Values in Simulated and Patient Data. *J. Nucl. Med.* **2017**, *58*, 387–392. [CrossRef]

61. Orlhac, F.; Soussan, M.; Maisonobe, J.A.; Garcia, C.A.; Vanderlinden, B.; Buvat, I. Tumor texture analysis in 18F-FDG PET: Relationships between texture parameters, histogram indices, standardized uptake values, metabolic volumes, and total lesion glycolysis. *J. Nucl. Med.* **2014**, *55*, 414–422. [CrossRef]

62. Kickingereder, P.; Gotz, M.; Muschelli, J.; Wick, A.; Neuberger, U.; Shinohara, R.T.; Sill, M.; Nowosielski, M.; Schlemmer, H.P.; Radbruch, A.; et al. Large-scale Radiomic Profiling of Recurrent Glioblastoma Identifies an Imaging Predictor for Stratifying Anti-Angiogenic Treatment Response. *Clin. Cancer Res.* **2016**, *22*, 5765–5771. [CrossRef] [PubMed]

63. Yasaka, K.; Akai, H.; Mackin, D.; Court, L.; Moros, E.; Ohtomo, K.; Kiryu, S. Precision of quantitative computed tomography texture analysis using image filtering: A phantom study for scanner variability. *Medicine (Baltimore)* **2017**, *96*, e6993. [CrossRef] [PubMed]

64. Harrell, F.E., Jr.; Lee, K.L.; Mark, D.B. Multivariable prognostic models: Issues in developing models, evaluating assumptions and adequacy, and measuring and reducing errors. *Stat. Med.* **1996**, *15*, 361–387. [CrossRef]

65. Vittinghoff, E.; McCulloch, C.E. Relaxing the rule of ten events per variable in logistic and Cox regression. *Am. J. Epidemiol.* **2007**, *165*, 710–718. [CrossRef] [PubMed]

66. Le, T.T.; Fu, W.; Moore, J.H. Scaling tree-based automated machine learning to biomedical big data with a feature set selector. *Bioinformatics* **2020**, *36*, 250–256. [CrossRef]

67. Virtanen, P.; Gommers, R.; Oliphant, T.E.; Haberland, M.; Reddy, T.; Cournapeau, D.; Burovski, E.; Peterson, P.; Weckesser, W.; Bright, J.; et al. SciPy 1.0: Fundamental algorithms for scientific computing in Python. *Nat. Methods* **2020**, *17*, 261–272. [CrossRef] [PubMed]

68. Bashir, A.; Brennum, J.; Broholm, H.; Law, I. The diagnostic accuracy of detecting malignant transformation of low-grade glioma using O-(2-[18F]fluoroethyl)-l-tyrosine positron emission tomography: A retrospective study. *J. Neurosurg.* **2018**, *130*, 451–464. [CrossRef]

69. Balagurunathan, Y.; Gu, Y.; Wang, H.; Kumar, V.; Grove, O.; Hawkins, S.; Kim, J.; Goldgof, D.B.; Hall, L.O.; Gatenby, R.A.; et al. Reproducibility and Prognosis of Quantitative Features Extracted from CT Images. *Transl. Oncol.* **2014**, *7*, 72–87. [CrossRef]

70. Grootjans, W.; Tixier, F.; van der Vos, C.S.; Vriens, D.; Le Rest, C.C.; Bussink, J.; Oyen, W.J.; de Geus-Oei, L.F.; Visvikis, D.; Visser, E.P. The Impact of Optimal Respiratory Gating and Image Noise on Evaluation of Intratumor Heterogeneity on 18F-FDG PET Imaging of Lung Cancer. *J. Nucl. Med.* **2016**, *57*, 1692–1698. [CrossRef]

71. Larue, R.T.; Defraene, G.; De Ruysscher, D.; Lambin, P.; van Elmpt, W. Quantitative radiomics studies for tissue characterization: A review of technology and methodological procedures. *Br. J. Radiol.* **2017**, *90*, 20160665. [CrossRef] [PubMed]

72. Wang, K.; Qiao, Z.; Zhao, X.; Li, X.; Wang, X.; Wu, T.; Chen, Z.; Fan, D.; Chen, Q.; Ai, L. Individualized discrimination of tumor recurrence from radiation necrosis in glioma patients using an integrated radiomics-based model. *Eur. J. Nucl. Med. Mol. Imaging* **2020**, *47*, 1400–1411. [CrossRef] [PubMed]

Publisher's Note: MDPI stays neutral with regard to jurisdictional claims in published maps and institutional affiliations.